Dry and Moist Idealized Experiments With a Two-Dimensional Spectral Element Model

SAŠA GABERŠEK *

UCAR/NRL, Monterey, California

FRANCIS X. GIRALDO

Naval Postgraduate School, Monterey, California

JAMES D. DOYLE

Naval Research Laboratory, Monterey, California

Corresponding author address: Saša Gaberšek, Naval Research Laboratory 7 Grace Hopper Avenue, Stop 2 Monterey, CA 93943-5502

E-mail: gabersek@ucar.edu

Report Documentation Page		*Form Approved* *OMB No. 0704-0188*

Public reporting burden for the collection of information is estimated to average 1 hour per response, including the time for reviewing instructions, searching existing data sources, gathering and maintaining the data needed, and completing and reviewing the collection of information. Send comments regarding this burden estimate or any other aspect of this collection of information, including suggestions for reducing this burden, to Washington Headquarters Services, Directorate for Information Operations and Reports, 1215 Jefferson Davis Highway, Suite 1204, Arlington VA 22202-4302. Respondents should be aware that notwithstanding any other provision of law, no person shall be subject to a penalty for failing to comply with a collection of information if it does not display a currently valid OMB control number.

1. REPORT DATE **2011**	2. REPORT TYPE	3. DATES COVERED **00-00-2011 to 00-00-2011**
4. TITLE AND SUBTITLE **Dry and Moist Idealized Experiments With a Two-Dimensional Spectral Element Model**		5a. CONTRACT NUMBER
		5b. GRANT NUMBER
		5c. PROGRAM ELEMENT NUMBER
6. AUTHOR(S)		5d. PROJECT NUMBER
		5e. TASK NUMBER
		5f. WORK UNIT NUMBER
7. PERFORMING ORGANIZATION NAME(S) AND ADDRESS(ES) **Naval Postgraduate School,Department of Applied Mathematics,Monterey,CA,93943**		8. PERFORMING ORGANIZATION REPORT NUMBER
9. SPONSORING/MONITORING AGENCY NAME(S) AND ADDRESS(ES)		10. SPONSOR/MONITOR'S ACRONYM(S)
		11. SPONSOR/MONITOR'S REPORT NUMBER(S)

12. DISTRIBUTION/AVAILABILITY STATEMENT **Approved for public release; distribution unlimited**

13. SUPPLEMENTARY NOTES

14. ABSTRACT

Two dimensional idealized dry and moist numerical simulations are performed and analyzed with a nonhydrostatic, fully compressible spectral element model. The dry numerical tests 4 consist of a linear hydrostatic mountain wave and a squall line is the basis for the moist simulations. A desired spatial accuracy with a spectral element model is determined by two 6 parameters, a number of elements (h) and a polynomial order (p) of the basis functions. In this paper, the range of average horizontal resolution varies from 0.2 km to 10 km. 8 Dry experiments are compared to an analytic solution for accuracy. It is found that the nominal resolution (x) of less than 2 km is su cient to minimize the error, while resolutions 10 of 500 m or less show no additional error reduction and are computationally expensive. When compared at a similar spatial resolution, the computational cost of the spectral element model 12 compared to a nite di erence model is an order of magnitude larger, but the accuracy gain is signi cant with the error an order of magnitude smaller for the spectral element model 14 when x is less than 1 km. If the acceptable error is known a priori, the spectral element model is less costly compared to the nite di erence model. 16 Evolution of a simulated squall line is compared across the h p space and evaluated with the help of three integrated quantities: total precipitation accumulation, maximum 18 vertical velocity and maximum precipitaton rate. The squall line is adequately resolved when the nominal resolution (x) is less than 2 km, but in addition, the polynomial order 20 (p) needs to be at least 5. The analysis of the integrated quantities across the parameter space consistently shows a gradient with respect to h at a xed p value (e.g. less rainfall 22 stronger maximum vertical velocities and weaker maximum rain rates with increasing h). The nonlinear nature of moist processes is responsible for this resolution dependence as a 24 result of localized buoyancy sources, evident in spectral analysis of the time and height averaged vertical velocity.

15. SUBJECT TERMS

16. SECURITY CLASSIFICATION OF:			17. LIMITATION OF ABSTRACT	18. NUMBER OF PAGES	19a. NAME OF RESPONSIBLE PERSON
a. REPORT **unclassified**	b. ABSTRACT **unclassified**	c. THIS PAGE **unclassified**	**Same as Report (SAR)**	**46**	

ABSTRACT

Two–dimensional idealized dry and moist numerical simulations are performed and analyzed with a nonhydrostatic, fully compressible spectral element model. The dry numerical tests consist of a linear hydrostatic mountain wave and a squall line is the basis for the moist simulations. A desired spatial accuracy with a spectral element model is determined by two parameters, a number of elements (h) and a polynomial order (p) of the basis functions. In this paper, the range of average horizontal resolution varies from 0.2 km to 10 km.

Dry experiments are compared to an analytic solution for accuracy. It is found that the nominal resolution ($\overline{\Delta x}$) of less than 2 km is sufficient to minimize the error, while resolutions of 500 m or less show no additional error reduction and are computationally expensive. When compared at a similar spatial resolution, the computational cost of the spectral element model compared to a finite–difference model is an order of magnitude larger, but the accuracy gain is significant with the error an order of magnitude smaller for the spectral element model when $\overline{\Delta x}$ is less than 1 km. If the acceptable error is known *a priori*, the spectral element model is less costly compared to the finite–difference model.

Evolution of a simulated squall line is compared across the h–p space and evaluated with the help of three integrated quantities: total precipitation accumulation, maximum vertical velocity and maximum precipitaton rate. The squall line is adequately resolved when the nominal resolution ($\overline{\Delta x}$) is less than 2 km, but in addition, the polynomial order (p) needs to be at least 5. The analysis of the integrated quantities across the parameter space consistently shows a gradient with respect to h at a fixed p value (e.g. less rainfall, stronger maximum vertical velocities and weaker maximum rain rates with increasing h). The nonlinear nature of moist processes is responsible for this resolution dependence as a result of localized buoyancy sources, evident in spectral analysis of the time– and height–averaged vertical velocity.

1

1. Introduction

Numerical models used for mesoscale weather forecasting can be assembled into two groups depending on the approach used to solve the governing Navier–Stokes equations. In the first group, the equations are kept in the differential form and both temporal and spatial derivatives are approximated using finite–differences (e.g. COAMPS, Hodur (1997), WRF, Skamarock et al. (2005), MM5, Dudhia (1993), MC2, Benoit et al. (1997), LM, Doms and Schättler (1997)). In the second group are methods based on an integral form, less frequently used in mesoscale forecasting, which includes spectral (Aladin, Bubnova et al. (1995)), pseudospectral, finite–element, spectral element and finite–volume models.

Spectral element models have been traditionally used in computational fluid dynamics and more recently also in computational geophysical fluid dynamics. For example, atmospheric phenomena have been studied on the global scale (e.g. Giraldo and Rosmond (2004); Fournier et al. (2004)), and more recently also on the mesoscale (Giraldo and Restelli 2008; Giraldo et al. 2010). Examples for the ocean include a density current model on a local scale (Özgökmen et al. 2004), and general circulation model (Dupont and Lin 2004; Curchitser et al. 1998).

Advances in high performance computing have led to substantial increase in the number of computational cores and to a smaller extent improved speed per core. Availability of computational resources is facilitating horizontal resolution refinement for the numerical weather prediction models on the global scale. In the future, one can foresee a natural merging of global and local area modelling efforts. Ideally, future unified models will have a flexibility to allow for varying resolution with grid refinements over areas of interest. In addition, the model should be able to utilize many cores and also scale well.

The spectral element (SE) method has the potential to meet this changing and challenging computational paradigm. This method provides a flexible platform, which supports unstructured grids and provides flexibility to adjust the accuracy of the dynamical core with a simple change of a control parameter. Moreover, the communication requirements in par-

2

allel processing are minimized because the adjacent elements share only the boundary points
with no additional interior points to be exchanged (Kelly and Giraldo 2011). An additional
novel characteristic of the SE model presented in this paper is the vertical discretization,
which is traditionally based on either a finite–element (Béland and Beaudoin 1985) or finite–
difference formulation (Kim et al. 2008). The model applied in this study is two–dimensional
and spectral element in both horizontal and vertical direction. To our knowledge, this is the
first fully compressible, nonhydrostatic spectral element model which also includes cloud
microphysics.

Previous studies using an SE model (Giraldo and Restelli 2008) have used a fixed set of
control parameters which control the domain decomposition: the number of elements in the
horizontal and vertical directions, h_x and h_z, respectively, and the polynomial order p (more
details in section 2). The purpose of this paper is to assess the strengths and weaknesses of a
SE model through the systematic exploration of the parameter space and validate simulation
results of two idealized mesoscale phenomena: a linear, hydrostatic mountain wave and mid–
latitude squall line.

In the first part of this paper, we use an analytic solution for a hydrostatic mountain
wave to validate the numerical simulations with the SE model. We address the following
questions: 1) What is the range of h–p parameters that give adequate results? 2) How
computationally expensive is the SE model compared to a typical finite–difference model?
3) How quickly does the SE model converge to the final solution?

In the second part, we assess the ability of the SE model to properly simulate the squall
line. Since there is no analytic solution, the typical approach with numerical simulations is to
increase both spatial and temporal resolution until convergence is achieved. This approach
might not be viable for atmospheric convection (e.g. Weisman et al. (1997), Bryan et al.
(2003)). Therefore we focus on the simulation of important characteristics (e.g. cloud forma-
tion, precipitation initiation, longevity of the storm system) of a squall line and integrated
quantities (e.g. average precipitation accumulation, maximum vertical velocity), across the

parameter space.

The structure of this paper is as follows: the model is described in Section 2; in Section 3 details of the experiment setup are given followed by discussion of results in Section 4. The conclusions are presented in Section 5.

2. Model Description

a. Governing Equations

The governing equations for the compressible, nonhydrostatic numerical model of the moist atmosphere are

$$\frac{\partial \rho'}{\partial t} + (\rho_0 + \rho')\nabla \cdot \boldsymbol{u} + w\frac{d\rho_0}{dz} + \boldsymbol{u} \cdot \nabla \rho' = 0 \qquad (1)$$

$$\frac{\partial \boldsymbol{u}}{\partial t} + \boldsymbol{u} \cdot \nabla \boldsymbol{u} + \frac{1}{\rho_0 + \rho'}\nabla p' + g\boldsymbol{k}(\frac{\rho'}{\rho_0 + \rho'} - 0.61q_v' + q_c + q_r) = \mu\nabla^2 \boldsymbol{u} \qquad (2)$$

$$\frac{\partial \theta_v'}{\partial t} + \boldsymbol{u} \cdot \nabla \theta_v' = S_{\theta_v'} + \mu\nabla^2 \theta_v', \qquad (3)$$

where air density (ρ), pressure (p), potential temperature (θ) water vapor mixing ratio (q_v) are separated into the vertically varying, hydrostatically balanced base state (subscript 0) and perturbation (denoted by prime): $\rho = \rho_0(z) + \rho'(\boldsymbol{x}, t)$. The wind vector has a horizontal and vertical component $\boldsymbol{u} = (u(\boldsymbol{x}, t), w(\boldsymbol{x}, t))^{\mathrm{T}}$, $\boldsymbol{k}$ is unit vector in vertical and g=9.81 m s^{-2} is the acceleration of gravity.

Moisture related variables are mixing ratios of water vapor (q_v), cloud water (q_c) and rain water (q_r). They are predicted according to a simple microphysical mechanism for a warm cloud, that does not include ice, snow and graupel, as follows

$$\begin{aligned}
\frac{dq_v}{dt} &= -C_c + E_c + E_r + \mu\nabla^2 q_v \\
\frac{dq_c}{dt} &= C_c - E_c - A_c - K_c + \mu\nabla^2 q_c \\
\frac{dq_r}{dt} &= A_c + K_c - E_r + F_r + \mu\nabla^2 q_r,
\end{aligned} \qquad (4)$$

where C_c is condensation of cloud water, E_c is evaporation of cloud water, E_r is evaporation

4

of rain water, A_c is autoconversion of cloud water into rain water, K_c is the collection of cloud water and F_r is the sedimentation of rain drops in the air parcel (Houze 1993). For a detailed description of each parameterized process see Klemp and Wilhelmson (1978).

The thermodynamic equation involves a source/sink term (S_{θ_v}) that describes latent heat release/uptake during phase changes of moisture variables. The momentum, thermodynamic and moisture equations involve a diffusion term. The diffusivity coefficient, $\mu = 200$ $\mathrm{m^2 s^{-1}}$, represents artificial viscosity terms used for numerical stability. Note that the diffusion is applied only for the moist sumulations. The pressure (p) and the virtual potential temperature (θ_v) are defined as

$$p \;=\; \rho R_d T(1 + 0.61 q_v) \tag{5}$$

$$\theta_v \;=\; (1 + 0.61 q_v) T \left(\frac{p_{00}}{p} \right)^{\frac{R_d}{c_p}} = (1 + 0.61 q_v)\theta, \tag{6}$$

with T being the air temperature, $p_{00} = 10^5$ Pa, reference air pressure, $R_d = 287$ J $\mathrm{kg^{-1}K^{-1}}$, a specific gas constant of dry air and $c_p = 1004$ J $\mathrm{kg^{-1}}$ specific heat at constant pressure for dry air.

b. Numerical model

Using the SE model, the computational domain Ω is decomposed into N_e nonoverlapping quadrilateral elements (Fig. 1, left panel)

$$\Omega = \bigcup_{e=1}^{N_e} \Omega_e. \tag{7}$$

Generally, the elements do not need to be quadrilateral and structured. A mapping from the global–domain coordinate system $\boldsymbol{x} = (x, z)$ onto the element–local (Ω_e) coordinate system $\boldsymbol{\xi} = (\xi, \eta)$ is described by an element–specific Jacobian $J = \frac{\partial \boldsymbol{x}}{\partial \boldsymbol{\xi}}$, where the local coordinates satisfy $(\xi, \eta) \in [-1, 1]^2$ (Fig 1, upper right panel).

The local element–wise solution of each variable f can be discretized using Nth order

polynomial basis

$$f^d(\boldsymbol{\xi}, t) = \sum_{k=1}^{K} \psi_k(\boldsymbol{\xi}) \hat{f}_k(t), \quad K = (N+1)^2, \tag{8}$$

where f^d is a discrete representation, ψ_k are expansion functions, $\hat{f}_k$ are expansion coefficients and $N+1$ is the number of expansion functions in each direction. The expansion functions (Fig 1, lower right panel) are constructed as

$$\psi_k = h_i(\xi(\boldsymbol{x})) \cdot h_j(\eta(\boldsymbol{x})), \quad i, j = 1, \dots, N+1, \tag{9}$$

where h_i and h_j are Lagrange polynomials

$$h_i(\xi) = -\frac{1}{N(N+1)} \frac{(1-\xi^2)P'_N(\xi)}{(\xi - \xi_i)P_N(\xi_i)}, \quad i = 1, \dots, N+1, \tag{10}$$

and $P_N(\xi)$ are Nth order Legendre polynomials. The expansion function h_i is zero at all nodal points except ξ_i. The chosen Legendre–Gauss–Lobato (LGL) grid points within the elements (ξ_i, η_j), are not equally spaced (Fig 1, upper right panel), but are given as the roots of

$$(1-\xi^2)P'_N(\xi) = 0. \tag{11}$$

The LGL points with the associated quadrature weights $\omega(\xi_i)$

$$\omega(\xi_i) = \frac{2}{N(N+1)} \left(\frac{1}{P_N(\xi_i)}\right)^2 \tag{12}$$

can be directly used for the Gaussian quadrature, approximating integrals over a local element Ω_e

$$\int_{\Omega_e} f(\boldsymbol{x})d\boldsymbol{x} = \int_{-1}^{1} \int_{-1}^{1} f(\xi, \eta) J(\xi, \eta) d\xi d\eta \simeq \sum_{i,j=1}^{N+1} \omega(\xi_i)\omega(\eta_j) f(\xi_i, \eta_j) |J(\xi_i, \eta_j)|. \tag{13}$$

The governing equations to be solved are in the form

$$\frac{\partial f}{\partial t} + F(f) = 0. \tag{14}$$

6

Substituting for the discretized solution will result in a residual

$$R(f^d) = \frac{\partial f^d}{\partial t} + F(f^d), \tag{15}$$

which can be minimized by various methods. In the Galerkin method, the residual is orthogonal to the expansion functions

$$(R, \psi_k) = 0, \quad k = 1, \ldots, (N+1)^2, \tag{16}$$

where the Legendre inner product (f, g) over the subdomain Ω_e is defined as

$$(f, g) = \int_{\Omega_e} f(\boldsymbol{x}) g(\boldsymbol{x}) d\boldsymbol{x}. \tag{17}$$

Combining (8), (15) and (16) leads to a system of differential equations

$$\sum_{n=1}^{(N+1)^2} I_{nk} \frac{d\hat{f}_k}{dt} = -\int_{\Omega_e} F \left(\sum_{n=1}^{(N+1)^2} \psi_n(\boldsymbol{\xi}) \hat{f}_n(t) \right) \psi_k d\boldsymbol{\xi}, \quad k = 1, \ldots, N+1. \tag{18}$$

The orthogonality of expansion functions simplifies the calculation of the mass matrix (I_{nk})

$$I_{nk} = (\psi_n, \psi_k) = \omega_n |J_n| \delta_{nk}. \tag{19}$$

The right hand side of (18) can be solved using the Gaussian quadrature. The spatial derivatives appearing in the governing equations are constructed through the analytic derivatives of the basis functions (for brevity only one–dimensional example is provided)

$$\frac{\partial f}{\partial x} = \frac{\partial f}{\partial \xi} \frac{\partial \xi}{\partial x} = \frac{\partial}{\partial \xi} \left(\sum_{k=1}^{N+1} \psi_k(\xi) \hat{f}_k(t) \right) \frac{\partial \xi}{\partial x} = \left(\sum_{k=1}^{N+1} \frac{\partial \psi_k(\xi)}{\partial \xi} \hat{f}_k(t) \right) \frac{\partial \xi}{\partial x}. \tag{20}$$

c. *Time integration*

The left hand side of (18) can be readily integrated in time with a desired accuracy. The nonuniform spacing of the nodal points can impose a severe constraint on a time step when using a regular explicit time integration scheme. For example, the ratio of the maximum to minimum nodal spacing for the tenth order polynomial expansion functions is almost five

7

and the maximum time step required for numerical stability is limited by the minimum nodal spacing. The terms in the governing equations can be rewritten in a compact vector form

$$\frac{\partial \boldsymbol{q}}{\partial t} = S(\boldsymbol{q}), \tag{21}$$

where $\boldsymbol{q} = (\rho', \boldsymbol{u}^{\mathrm{T}}, \theta_v, q_v, q_c, q_r)^{\mathrm{T}}$, and S represents all terms not involving time derivatives. The semi-implicit time integration can be introduced in the previous equation as

$$\frac{\partial \boldsymbol{q}}{\partial t} = \{S(\boldsymbol{q}) - \lambda L(\boldsymbol{q})\} + [\lambda L(\boldsymbol{q})], \tag{22}$$

where curly and square braces represent explicit and implicit integration, respectively, $\lambda = \{0, 1\}$ is a control flag to invoke the implicit integration ($\lambda = 1$), and L is a linear approximation of S that contains acoustic and gravity waves. The moisture related variables are not responsible for either fast mode, so the linearized formulation contains only the first four components of $\boldsymbol{q}$

$$L(\boldsymbol{q}) = \begin{pmatrix} -w\frac{d\rho_0}{dz} - \rho_0 \nabla \cdot \boldsymbol{u} \\ -\frac{1}{\rho_0}\frac{\partial p'}{\partial x} \\ -\frac{1}{\rho_0}\frac{\partial p'}{\partial z} - g\frac{\rho'}{\rho_0} \\ -w\frac{d\theta_{v0}}{dz} \end{pmatrix}. \tag{23}$$

Instead of solving for each variable separately, they are combined into one pseudo–Helmholtz equation for the pressure perturbation (Schur complement). Upon solving for the pressure, each of the prognostic variables can be solved in sequence for the updated variables (Giraldo et al. 2010). The time integrator is the second order backward difference method, BDF2 (Giraldo 2005). It is used in a semi–implicit mode permitting longer time steps compared to fully explicit methods with equal or higher order of accuracy which have also been tested (e.g. family of Runge–Kutta schemes).

As in most numerical models involving moist processes solved with a finite–difference scheme in the vertical, the microphysics computation is time–integrated separately to allow a time step adjustment for the case when sedimentation of precipitable water is too fast.

8

Moist processes are treated in a column–wise fashion, descending from the top of the domain to the lowest level, moving laterally through the domain. The indexing of the elements, and all the loops in the source code can be completely unstructured and therefore not readily applicable for microphysics calculations. For the purposes of this paper, the element-wise thermodynamic and moist variables are mapped to regular two–dimensional arrays suitable for column–wise calculations. Once the microphysics computations are concluded, the updated variables are mapped back onto their local elements. As such, the actual microphysical processes are not strictly computed within the semi–implicit realm, but the advection and diffusion of the moisture related variables are.

d. Accuracy

When using a polynomial expansion basis, one frequently refers to it only by its order. It should be emphasized that this is not the same 'order' as the one used to identify the leading term of the error when using finite–difference schemes, which in fact describes accuracy. Evaluation of Gaussian quadrature (RHS of (18)) over $N+1$ quadrature points, will be exact to machine precision as long as the polynomial integrand is of the order $2 \cdot (N+1) - 3$, or less (Karniadakis and Sherman 2005). Applying the SE method to the governing equations will result in an inner product of two polynomials of the same (or lesser) degree. For example, the product $u \frac{\partial \rho'}{\partial x}$, subject to the orthogonality condition is of the $3N - 1$ order. For the exact integration, at least $\frac{3}{2}N + 1$ points are needed, while only $N + 1$ are available. The integrand is subsampled and consequently aliased. To eliminate this aliasing, a low–pass filter is applied, but not directly to the chosen expansion functions because they are nodal. They are transformed into modal functions first, filtered using a Boyd–Vandeven filter (Giraldo and Rosmond 2004) and inversely transformed to retrieve a filtered set of nodal expansion functions. The inexact integration has a very minimal impact for higher order polynomials ($N \geq 4$) (Giraldo 1998). Note that an exact integration could be achieved by using a separate set of quadrature points, but the accompanying computational cost is usually prohibitive

9

due to the mass matrix no longer being diagonal. The errors stemming from the BDF2 time integration are of second order accuracy.

3. Setup and Initial Conditions

The model is applied in a two–dimensional mode with a horizontal and vertical domain of 240 and 24 km, respectively. Due to the irregular spacing of nodal points within an element in both the horizontal and vertical directions, a nominal resolution is introduced, defined as the element's extent divided by the number of nodal points (minus one) in that direction. When describing a simulation, its corresponding nominal horizontal and vertical resolution are provided. The discrepancy between the actual adjacent nodal point spacing and the associated nominal resolution increases with the polynomial order.

The desired nominal resolution can be achieved by increasing the number of elements (h) while holding the polynomial order (p) constant ('h–refinement'), keeping the element number constant and increasing the polynomial order ('p-refinement'), or varying both. The limiting 'h-refinement' case is a finite–element method (high h, low p), while a similar limit for the 'p-refinement' is a spectral method (one element, high number of basis functions).

When investigating the resolution dependence of the SE model, one has to consider exploration of the phase space defined by both parameters: the polynomial order and number of elements. In order to achieve a nominal horizontal resolution representative for a mesoscale model we choose the polynomial order to vary between 4 and 10 and the number of elements in the horizontal direction between 6 and 120. The resulting nominal grid spacing varied between 200 and 10000 m in 91 simulations overall (see Table 1 for details).

Note that the same refinement applies to both the horizontal and vertical directions. It may be desirable to keep the nominal vertical resolution constant in all experiments, such as in Weisman et al. (1997), to focus solely on the effects of variations in the horizontal resolution. This not practical to two reasons: i) the polynomial order is the same in both

10

directions in the current version of the model, and ii) the number of elements can be an integer number only. The impact of varying the nominal vertical resolution is briefly examined in section 4 and shown to have significant impact as long as the nominal vertical resolution is sufficient to adequately resolve the squall line cold pool. The ratio of nominal horizontal and vertical resolution is thus kept in the same range (1:3-1:5) in all simulations.

a. Dry Experiments – Linear, Hydrostatic Mountain Wave

In the first suite of experiments, we focus on the case of a linear hydrostatic gravity wave generated by flow over small topography. The topography $h(x)$ is defined with a bell shaped profile

$$h(x) = \frac{h_m a^2}{x^2 + a^2}, \tag{24}$$

where $h_m = 1$ m is the terrain height and $a = 10.0$ km is the mountain half–width. In an isothermal atmosphere ($T_0 = 250.0$ K) the atmospheric stability is constant with height ($N = \frac{g}{\sqrt{c_p T_0}} = 0.0196$ s^{-1}). By choosing an appropriate wind speed ($\bar{u} = 20.0$ m/s) both conditions for hydrostacity ($Na/\bar{u} \gg 1$) and linearity ($Nh_m/\bar{u} \ll 1$) are satisfied. The computational domain is 240 km wide and 24 km deep. An active sponge layer at the lateral and top boundaries helps to damp reflections from the domain boundaries. Since the width of the lateral sponge is proportional to the nominal horizontal grid spacing, the domain extent is doubled horizontally for all cases with the nominal grid spacing greater than 4 km. All simulations are performed using the semi-implicit time integrator. Each simulation is integrated for 12 hours (nondimensional time $\bar{u}t/a = 86.4$), assuring that a steady state is reached.

b. Moist Experiments – Squall Line

The initial conditions are specified by a synthetic vertical profile (Fig. 2), based on a typical environment for midlatitude squall lines and used in several previous studies (Rotunno

11

et al. 1988). It features increasing moisture in the lower troposphere and a fairly moist but unsaturated air mass in the rest of the troposphere. The air is weakly stable close to the ground with uniform stability (N=0.01 s^{-1}) up to the tropopause at 12 km where the stability increases (N=0.02 s^{-1}). A low–level wind shear is added to promote longevity of the storm by separating the storm inflow from the downdraft created by precipitation. In addition, if the horizontal component of vorticity of the environmental shear is approximately balanced by the vorticity of the opposite sign, created by the density current of the outflow, the storm will remain quasi–stationary (Rotunno et al. 1988). The topography is set to zero for the moist experiments, there is a sponge layer at the top of the domain, identical to the dry simulations, but at the lateral boundaries we use periodic boundary conditions. The main reason for choosing periodic lateral boundary conditions is to evaluate mass conservation during the simulation.

The triggering mechanism for the storm evolution is a warm bubble (Rotunno et al. 1988), centered at the height of 2 km, inserted at the initial time. The temperature perturbation is defined as

$$
\Delta\theta \;=\; \begin{cases} \theta_c \cdot \cos^2 \frac{\pi r}{2}, & r \leq r_c \\ 0, & r > r_c \end{cases} \tag{25}
$$

$$
r \;=\; \sqrt{(\frac{x - x_c}{x_r})^2 + (\frac{z - z_c}{z_r})^2}, \tag{26}
$$

where θ_c=3.0 K, x_c=0, z_c=2, x_r=10, z_r=1.5 and r_c=1.0 km. The perturbation reaches its maximum value at the center (x_c, z_c) and decreases radially outward. The triggering mechanism is different from the density current used by Weisman et al. (1997). Due to the periodic boundary conditions used in our simulations, the density current would enter the domain from the upstream and cause an unwanted secondary line of storms.

The initial positive buoyancy perturbation initiates air parcel ascent. Once they reach the level of free convection, the lifting continues as long as the parcels are less dense than the surroundings, described by the Convective Available Potential Energy (CAPE), summarized in Table 2. Values in excess of 2000 J kg^{-1} suggest the possibility of a strong convective

12

activity.

4. Results

a. Dry Experiments – Linear, Hydrostatic Mountain Wave

We explore the $h - p$ parameter space through analysis of the inviscid (i.e. no artificial viscosity $\mu = 0$), linear, hydrostatic mountain wave simulations, for which an analytic solution exists. Instead of calculating error statistics for the model variables separately, the model performance is assessed by calculating a second order quantity, the momentum flux, as a function of height, M_z, and compared to the analytic height–independent solution (M^a) (Durran and Klemp 1983)

$$M_z = \int_{-\infty}^{\infty} \bar{\rho}(z)u'(z)w(z)dx \tag{27}$$

$$M^a = -\frac{\pi}{4}\rho_0 N\bar{u}h_m^2 = -0.4285 \text{ kg s}^{-2}, \tag{28}$$

where $\rho_0 = 1.3937$ kg m^{-3} is the air density at the surface and the u–component of velocity is decomposed into the mean state and perturbation ($u = \bar{u} + u'$). Due to the small terrain height (h_m), the quadratures calculated at a constant height z (M_z) or at a constant model level k (M_k) are essentially the same. While evaluating the integrals, the lateral portions of the domain with an active sponge are omitted. The normalized l_2 norm is calculated using M_k and M^a for all the model levels from the ground ($k = 1$) to the uppermost level not affected by the top sponge ($k = k_s$)

$$l_2 = \sqrt{\frac{\sum_{k=1}^{k=k_s}(M_k - M^a)^2}{\sum_{k=1}^{k=k_s}(M^a)^2}}. \tag{29}$$

Simulations with higher nominal resolution ($\overline{\Delta x} \leq 1$ km) have the smallest error statistics (right portion of Fig. 3). Cases with lower nominal horizontal resolution ($\overline{\Delta x} \geq 5$ km) and polynomial order ($p \leq 6$) result in relatively poor l_2 statistics (lower left portion of Fig.

3), due to a combined effect of the poorly resolved topography and error introduced with inexact integration (Eqn. (13)) for lower polynomial orders.

A smaller subset of cases (shaded in gray in Table 1) is further analyzed to assess the speed of convergence and computational cost as a function of the polynomial order (p=4, 6, 8 and 10) and number of elements (h), reflected in the nominal horizontal resolution ($\overline{\Delta x}$=0.5, 1.0, 2.0 and 3.0 km). In addition, accuracy, convergence and timing comparisons for a finite–difference (FD) model (fully compressible, nonhydrostatic with a fourth order horizontal advection, for more details see Durran and Klemp (1983)) are used with the same domain and with the matching horizontal and vertical grid spacings.

A reduction of the l_2 error at a particular point on Fig. 3 can be achieved by increasing the polynomial order (p–refinement), increasing the number of elements (h–refinement) or both. Keeping the relatively coarse nominal resolution constant ($\overline{\Delta x}$=2.0, 3.0 km) and increasing p yields only minor error reduction (compare dotted and dash–dotted lines of various shades of gray in Fig. 4). There is not much change in the l_2 error past t=5 hours regardless of the polynomial order, which suggests that the nominal resolution is too coarse for an accurate solution of the mountain wave. Starting with a finer resolution ($\overline{\Delta x}$=0.5 or 1.0 km) the error continues to decrease and it is at least an order of magnitude smaller compared to the previously analyzed set of cases with coarser resolution, regardless of the polynomial order. Note that while the errors for the $\overline{\Delta x}$=1.0 km set reach minima at t=11 h, they are still decreasing at the end of the simulation time for the $\overline{\Delta x}$=0.5 km set. For the finite–difference model (lines with diamonds in Fig. 4), increasing the spatial resolution and decreasing the time step results in a more monotonic error reduction. Even at the highest resolution (solid line with diamonds on Fig. 4) the error, dominated by the lowest–order truncation term, is still at least an order of magnitude larger compared to the SE model (solid lines on Fig. 4). Note that the error lines for the simulations with p=10 indicate the error is still decreasing after 12 hours of simulation, previously observed by Giraldo and Restelli (2008).

Improving accuracy by using more elements (better resolution) is computationally more

14

costly. Wallclock time for the SE model increases approximately by an order of magnitude, as the resolution gets refined from $\overline{\Delta x}$=2.0 to $\overline{\Delta x}$=1.0 km and similarly from $\overline{\Delta x}$=1.0 to $\overline{\Delta x}$=0.5 km (Fig. 5). Variations within each cluster of points are due to the polynomial order, where the lowest order is the least expensive (compare matching symbols with different shades of gray in Fig. 5). The finite–difference model is computationally less expensive compared to the SE model, when comparing timing results for matching nominal spacing $(\overline{\Delta x})$ for the SE model with the constant spacing (Δx) for the FD model. Note, however, that if we change the comparison metric to a desired value of l_2 error, the SE model is faster. Moreover, at the same computational cost, the l_2 error associated with the SE model is for the values of $\overline{\Delta x} \leq 1$ km at least an order of magnitude smaller compared to the FD model. The error reduction is gradual with increasing resolution for the FD model (solid line with triangles), while the major error reduction for the SE model occurs with a refinement from $\overline{\Delta x}$=2.0 to $\overline{\Delta x}$=1.0 km (Fig. 5). The integration time steps used for both models are at a maximum allowed from a numerical stability perspective.

To summarize the dry experiments, the resolution required to adequately resolve the simulated phenomenon can be achieved by either h or p refinement. At a fixed nominal resolution the error is almost always the largest for the lowest polynomial order, p=4, represented by black lines in Fig. 4. Our recommendation is therefore for the polynomial order to be at least p=6. Higher values of p come with increasing computational cost, perhaps prohibitively expensive for p=10, with the best ratio of accuracy and resources spent is achieved at p=8. The number of operations for a two–dimensional SE model described in this paper is on the order of $\mathcal{O}(N_e \cdot p^3)$, with N_e being the total number of elements (a product of number of elements in the horizontal and vertical). As the resolution refinement scales as $\mathcal{O}(N_e \cdot p)$, it is computationally more feasible to increase the number of elements, since the cost increases cubically with p. With the fixed nominal resolution, the ratio of the most expensive (p=10) to the least expensive (p=4) simulation is 2.5, which can be calculated from the table 1 and confirmed on Fig. 5.

b. Moist Experiments – Squall Line

A brief synopsis of the storm evolution is based on a simulation with a typical mesoscale resolution with $\overline{\Delta x}$=1 km and $\overline{\Delta z}$=0.2 km, which corresponds to a case with p=8 and h=30. After the initialization, the first cloud forms at around t=900 s (Fig. 6a), the cloud keeps growing with warm microphysical processes resulting in rain formation, which starts accumulating at the surface at around t=1800 s (Fig. 6b). By t=4800 s, a strong cold pool has formed at near the rear of the storm, characterized by negative equivalent potential temperature perturbation, caused by evaporative cooling by rain water and downward motion of cooler air from aloft (Fig. 6c). The cold pool spreads as a density current at the surface and if the induced shear and associated horizontal component of vorticity are not exactly balanced by the ambient shear, the squall line will propagate. New updrafts are being formed in the upshear region (ahead of the location of the original initiation) as the density current initiates forced lifting (secondary triggering mechanism), consistent with a broadening region of accumulated precipitation and downshear tilt of the convective tower (Fig. 6d). The subsequent triggered convection is generally weaker compared to the initial onset.

We start examining the results across the h–p parameter space by inspecting simulations with the same nominal resolution $\overline{\Delta x}$=1 km, at t=6000 s (Figs 7a-f). Overall, the cloud structure (anvil extent, downshear tilt of the convective tower), the cold pool intensity and precipitation amount are similar among the simulations. The most significant difference among the simulations is the spatial distribution of the rainfall accumulation and related lateral extent of the cold pool beneath the cloud. The only differences in the setup among the cases are the polynomial order p and the number of elements in the horizontal direction h, resulting in a variable nodal spacing where the ratio of the maximum to minimum nodal spacing ranges from 1.9 (p=4, Fig. 7a) to 8.8 (p=20, Fig. 7f). Note that the last case with high value of p is not described in Table 1. Three additional experiments are designed with p=20. The number of horizontal and vertical elements is 6/3, 12/6 and 24/12, resulting in nominal resolutions of 2.0, 1.0 and 0.5 km, respectively (not in Table 1). Despite the ratio of

16

the narrowest to the widest nodal spacing within the element is O(0.1) (Table 3), the overall storm is still well resolved (Fig. 7f). The rapidly varying nodal spacing, in addition to large differences between the widest and narrowest nodal distance, does not result in preferred location for convection or "single–cell" storms or updrafts.

The similarity among the snapshots of the squall line simulation across the h–p parameters with the same nominal spatial resolution extends the robustness of the SE model beyond the dry, dynamical core tests shown in the previous section. The disagreement in the total precipitation accumulation is discussed later in this section.

Adequately resolved storms (cases with $\overline{\Delta x} < 3$ km) undergo similar stages of development, but differ in the accumulated precipitation amount, as shown by a series of four simulations with the same polynomial order (p=8). The nominal resolution starts at $\overline{\Delta x}$=3 km and is progressively reduced by factors of two down to 0.375 km (Fig. 8). The simulation with the coarsest nominal resolution has an excessive amount of precipitation with an overall cloud outline similar to the shape at the higher resolution (Fig. 8a). As the resolution increases, the overall precipitation amount decreases, the spatial extent of the cold pool is reduced, although the strength is comparable, and the size of the cloud gets smaller (Figs.8 b-d).

Without an existing analytic solution for comparison purposes, we assess the moist simulation using metrics appropriate for convective events: total rain accumulation, maximum rain rate and maximum vertical velocity. Simulations with a poorly resolved triggering thermal bubble, which never develop any convection are assigned zeros for all validation parameters. These simulations are clustered in the lower left portion of the h-p parameter space (Figs 9a-c). In addition, cases filling the rest of the void region share in common the *maximum* nodal spacing being larger than 4 km (the actual limiting contour is between the $\overline{\Delta x}$=2.5 and 3 km contours). This latter group of cases grossly overpredicts the precipitation (Fig 8a) and all the validation parameters are assigned zeros. A threshold value of minimum grid spacing required for an adequately resolved squall line is similar to that for the FD

17

models (Weisman et al. 1997), despite the difference in uniformity of grid points between the SE and FD model.

The total rain accumulation for the duration of the simulation, averaged over the whole domain (Fig. 9a) indicates a decrease with increasing h. The negative correlation between the precipitation accumulation and nominal resolution is also apparent when comparing simulations with the same p (Figs. 8a-d). Note that the gradient is somewhat independent of the polynomial order. The reduction of the rain accumulation is consistent with findings of Weisman et al. (1997) where simulations with coarser resolution tended to exhibit slower evolution, stronger storm circulation and higher overall precipitation amounts. The maximum rain rate (Fig. 9b) is reduced with increasing h, which is consistent with the reduction of the total precipitation accumulation at higher resolution. A comparison of the maximum vertical velocities indicates they are in the range between 20 and 30 m s^{-1} (Fig. 9c), similar to values reported by Bryan et al. (2006) and Weisman and Rotunno (2004). There is a noticeable trend of higher maximum vertical velocities (in excess of 30 m s^{-1}) with increasing nominal resolution. The apparent inconsistency with the reversed trend in vertical velocities, compared to previously observed gradients of precipitation accumulation and maximum rain rate, is due to scaling of the maximum rain rate by the corresponding nodal spacing. If similar scaling is applied to the vertical velocities, as a proxy for the vertical mass flux, there is again a reduction in values with increasing resolution (not shown).

A trend that can be recognized from Figs 9a-c suggests that results are more dependent on the h than p refinement and that the gradient with respect to h is consistent for all analyzed quantities. These conclusions differ from Weisman et al. (1997), but in their study the finest resolution is 1 km, the horizontal grid spacing is constant and more importantly, the sub–gridscale mixing is parameterized.

For dry simulations of a density current with increasing resolution (Straka et al. 1993), the solutions are converging towards the solution obtained with the finest resolution. Mixing has a strong effect on the overall evolution of the storm. When utilizing a sub–gridscale

18

physical mixing that scales with the horizontal resolution, a certain degree of convergence of solutions can be expected when spanning a wide range of horizontal resolutions (Weisman et al. 1997). If the resolution is progressively refined, the results might become different to some extent as documented by Bryan et al. (2003) and in this paper. We hypothesize that the nonlinear character of the moist processes leads to this behavior. The spatial and temporal distributions of buoyancy perturbations depend on localized phase changes, which will differ among simulations with different nodal point distribution. To explore this issue further, we ran an additional set of cases (p=8, increasing h) based on the setup for the squall line simulations, except with no moisture at the initial time. We calculated power spectra of vertical velocities, averaged in time and height, as a function of horizontal wavelength. Since the model data is on a nonuniformly spaced grid, it is resampled with the horizontal spacing that approximates the narrowest nodal spacing. If the above hypothesis holds, the spectra for the "dry" squall line simulations should converge. The power spectra peaks are at the same wavelength and the spectra width do not change with the resolution (Fig. 10b), except for the case with $\overline{\Delta x}$=3 km, which poorly resolves the initial thermal bubble. For the original squall line simulations, there is a broadening of the power spectra and a shifting of the maxima towards the shorter wavelengths with increasing nominal resolution (Fig. 10a). Whether this trend continues or if the spectra collapse with further resolution refinement is beyond the scope of this research. In a separate subset of experiments (p=8, increasing h) with no latent heat release or uptake permitted, the cloud shapes are almost exactly the same independent of the spatial resolution.

The average time between sequential discrete updrafts is determined by local maxima in positive vertical velocities. The time is well within the documented range of Rotunno et al. (1988), corresponding to their "optimal state", except when the nominal resolution is less than 1 km the average time becomes longer, because the subsequent convective cells take longer time to form. In addition, the time between the initial storm triggering and rain reaching the ground is consistent with findings in the literature (Weisman et al. 1997)

throughout the parameter space (not shown), suggesting that the choice of h–p parameters does not affect the storm triggering by the initial buoyancy perturbation.

One of the concerns when simulating severe convection using a variable grid is development of preferential locations for convection, manifested by extrema in vertical velocities. To test the uniformity of the spatial distribution of vertical momentum, we combined the vertical velocities at each cell into 0.5 m s^{-1} bins in the range $[4.75, 20.75[$ m s^{-1}, for all the available output times. Next, bins of all vertical cells at a fixed horizontal distance are combined, resulting in a two-dimensional histogram revealing a spatial distribution of occurrence for a particular vertical velocity bin (not shown). Most of the motions with higher absolute vertical velocities are occurring in the eastern part of the domain, as expected, where the squall line slowly propagates. There is no visible evidence of convection triggering at preferred locations (narrowest nodal spacing next to the element boundaries). Furthermore, bins of all the cells with the same horizontal dimension are combined and normalized to obtain a relative frequency histogram as a function of the vertical velocity (not shown). If the convection is indeed taking place closer to the element boundaries where the nodal spacing is at a minimum, this would manifest itself in the histogram by a higher (lower) relative frequency of the narrower (wider) cells, which is not the case.

As mentioned in section 3, the number of elements can be independently set in both directions, changing the respective nominal resolution. We designed a small subset of four experiments based on a case with p=10 and $\overline{\Delta x}$=1 km to assess the effect of varying nominal vertical resolution with the nominal horizontal grid spacing held constant. The number of elements in the vertical direction is 4, 10, 20 and 40, resulting in nominal vertical resolution of 600, 240, 120 and 60 m, respectively. The horizontal location of the most intense convection, the magnitude of the maximum updraft and the overall precipitation accumulation are not sensitive to the vertical resolution.

In a series of additional tests, sensitivity to domain length, symmetry, wind shear and viscosity are investigated. The choice of periodic boundary conditions does not have a sig-

nificant impact on the results, when compared to simulations with triple the domain length. With no ambiental wind shear, a symmetric storm cloud is expected, but an asymmetry can develop if the initial thermal bubble perturbation is not centered exactly over the symmetric nodal points. If the wind shear is too strong, no storm develops, similar to findings of Rotunno et al. (1988) and Weisman et al. (1988). Small values of viscosity ($\mu<5$ m^2 s^{-1}) can lead to numerical instabilities, while large values ($\mu>750$ m^2 s^{-1}) inhibit convective activity.

5. Conclusions

In this paper we examine the characteristics of a two–dimensional spectral element (SE) model for dry and moist mesoscale atmospheric test cases: a linear, hydrostatic mountain wave and a squall line, respectively.

There are two parameters that control the setup of the SE model: the number of elements into which the computational domain is subdivided, and polynomial order of the basis functions (p), which determines the number of nodal points within the element. The spatial resolution for the SE model is determined by the choice of the two parameters with ranges from 4 to 10 (p) and 6 to 120 (number of elements in horizontal, h), resulting in the average horizontal (vertical) resolution ranging from 200 (40) to 10000 (1500) m, and a total of 91 simulations spanning the h–p parameter space.

For the linear hydrostatic mountain wave case,an analytic solutionis used to validate the model performance. Generally, cases with the nominal resolution less than 2 km yield the best results, with no significant gain in accuracy if the resolution is refined beyond 1 km. The least skillful results are attributed to coarse resolution, not sufficient to resolve the mountain barrier, and to the low polynomial order, which contributes to the error when using the inexact integration. Simulations with coarser nominal resolution converge faster towards the steady state solution, but with larger error. In addition, the SE model results are compared to solutions obtained by a finite–difference (FD) model with matching spatial resolutions,

21

for accuracy and timing purposes. The error for the FD simulations monotonically decreases with refined spacing, but even with the finest grid spacing (0.5 km), the error is an order of magnitude larger compared to the fine resolution cluster of the SE model. At a given resolution, matching the nominal spacing ($\overline{\Delta x}$) of the SE model with the constant spacing (Δx) of the FD model, the SE model is approximately an order of magnitude more computationally expensive than the FD model. The situation is reversed, if a specified error is desired – the SE models is less expensive. Moreover, the error of the SE model for the nominal spacing $\overline{\Delta x} \leq 1$ km is an order of magnitude lower compared to the FD model at the same resolution. The computational cost as a function of the grid spacing and associated time step increases almost uniformly for the FD model, while there is almost no improvement in error with associated computational cost when increasing the nominal resolution from 3 to 2 km or from 1 to 0.5 km for the SE model. The best improvement occurs when the resolution is refined from 2 to 1 km.

Simulations that adequately resolve the initial warm bubble perturbation for the squall line case, successfully simulate the upscale transition from a local, isolated convective cell into a mesoscale, organized storm system. The results of the main set of moist experiments and additional sensitivity tests suggest the overall ability of the SE model to adequately simulate the squall line. Increasing the nominal resolution below 1 km leads to some differences. Qualitatively, the cloud shapes are very similar, but simulations with the finest nominal resolution tend to produce stronger maximum vertical velocities with more localized and reduced precipitation accumulation. We hypothesize and offer evidence that this behavior can be explained by a nonlinear nature of latent heating and localization of buoyancy sources. A comparison of averaged power spectra of vertical velocity for the original squall line simulations and a modified set with no initial moisture indicates shifting of the power spectra toward smaller scales for the moist cases, when the resolution is refined. How would a continuing resolution refinement affect power spectra for the original squall line remains an open question. At this point simulations with very high spatial resolution are

computationally too expensive to run with a serial code.

The SE model supports both structured and unstructured grids. The accuracy can be adjusted with the same code by choosing the control parameters (h and p). Unlike the numerical models that use the terrain–following vertical coordinate, the SE model can handle complex topographical features with extreme slope angles, such as in urban environments. For all these advantages, there is a price to pay. The source code is generally less straightforward to understand compared to the source code of the FD models. As mentioned earlier, the SE models are computationally more expensive compared to the FD models, when used at the same spatial resolution.

A recommended subspace of the h–p parameter space depends on a compromise among acceptable error, computational cost, and required resolution to resolve the feature of choice. Based on our results for inviscid, dry, and viscous, moist simulations of the mesoscale phenomena, which are dimensionally similar, the nominal resolution should be within the $\overline{\Delta x}$=0.5-2 km range and the polynomial order in the range p=5-10. This study is to our knowledge the first attempt to systematically map the h–p parameter space for using the SE model in mesoscale atmospheric modeling.

The results are certainly encouraging enough to warrant further investigations in using the SE model for more realistic mesoscale atmospheric modeling scenarios. The model in its dry and inviscid form is currently being tested in three dimensions and on massively–parallel computers. This will allow us to extend the parameter space to include very fine spatial resolutions which are prohibitively expensive in the serial mode. In the future, we plan to adapt the microphysics scheme to three dimensions, expand it to include the ice phase and implement a sub–gridscale mixing parameterization.

REFERENCES

Béland, M. and C. Beaudoin, 1985: A global spectral model with a finite element formulation for the vertical discretization: Adiabatic formulation. *Monthly weather review*, **113**, 1910–1919.

Benoit, R., M. Desgagné, P. Pellerin, S. Pellerin, Y. Chartier, and S. Desjardins, 1997: The Canadian MC2: A Semi-Lagrangian, Semi-Implicit Wideband Atmospheric Model Suited for Finescale Process Studies and Simulation. *Monthly Weather Review*, **125 (10)**, 2382.

Bryan, G. H., J. C. Knievel, and M. D. Parker, 2006: A Multimodel Assessment of RKW Theory's Relevance to Squall-Line Characteristics. *Monthly Weather Review*, **134 (10)**, 2772–2792.

Bryan, G. H., J. C. Wyngaard, and J. M. Fritsch, 2003: Resolution Requirements for the Simulation of Deep Moist Convection. *Monthly Weather Review*, **131 (10)**, 2394.

Bubnova, R., G. Hello, P. Benard, and J.-F. Geleyn, 1995: Integration of the Fully Elastic Equations Case in the Hydrostatic Pressure Terrain-Following Coordinate in the Framework of the ARPEGE/Aladin NWP System. *Monthly Weather Review*, **123**, 515–535.

Curchitser, E. N., M. Iskandarani, and D. B. Haidvogel, 1998: A Spectral Element Solution of the Shallow-Water Equations on Multiprocessor Computers. *Journal of Atmospheric and Oceanic Technology*, **15 (2)**, 510–521.

Doms, G. and U. Schättler, 1997: The Nonhydrostatic Limited-Area Model LM (Lokal-Modell) of DWD. Part I: Scientific Documentation.

Dudhia, J., 1993: A nonhydrostatic version of the Penn State/NCAR Mesoscale Model:

Validation tests and simulation of an Atlantic cyclone and cold front. *Monthly Weather Review*, **121**, 1493–1513.

Dupont, F. and C. a. Lin, 2004: The Adaptive Spectral Element Method and Comparisons with More Traditional Formulations for Ocean Modeling. *Journal of Atmospheric and Oceanic Technology*, **21 (1)**, 135.

Durran, D. R. and J. B. Klemp, 1983: A compressible model for the simulation of moist mountain waves. *Monthly Weather Review*, **111 (12)**, 2341–2361.

Fournier, A., M. A. Taylor, and J. J. Tribbia, 2004: The spectral element atmosphere model (SEAM): High-resolution parallel computation and localized resolution of regional dynamics. *Monthly Weather Review*, **132 (2002)**, 726–748.

Giraldo, F. X., 1998: The Lagrange-Galerkin Spectral Element Method on Unstructured Quadrilateral Grids. *Journal of Computational Physics*, **147 (1)**, 114–146.

Giraldo, F. X., 2005: Semi-implicit time-integrators for a scalable spectral element atmospheric model. *Quarterly Journal of the Royal Meteorological Society*, **131 (610)**, 2431–2454.

Giraldo, F. X. and M. Restelli, 2008: A study of spectral element and discontinuous Galerkin methods for the Navier-Stokes equations in nonhydrostatic mesoscale atmospheric modeling: Equation sets and test cases. *Journal of Computational Physics*, **227**, 3849–3877.

Giraldo, F. X., M. Restelli, and M. Läuter, 2010: Semi-implicit formulations of the Navier-Stokes equations: application to nonhydrostatic atmospheric modeling. *SIAM J. Sci. Comp.*, **32 (6)**, 3394–3425.

Giraldo, F. X. and T. E. Rosmond, 2004: A Scalable Spectral Element Eulerian Atmospheric Model (SEE-AM) for NWP: Dynamical Core Tests. *Monthly Weather Review*, **132 (1)**, 133–153.

26

Hodur, R. M., 1997: The Naval Research Laboratory's Coupled Ocean/Atmosphere Mesoscale Prediction System (COAMPS). *Monthly Weather Review*, **125**, 1414–1430.

Houze, R. A., 1993: *Cloud Dynamics*. Academic Press.

Karniadakis, G. E. and S. Sherman, 2005: *Spectral/hp Element Methods For Computational Fluid Dynamics*. Oxford Science Publications.

Kelly, J. F. and F. X. Giraldo, 2011: Development of the nonhydrostatic unified model of the atmosphere (numa): Limited area mode. *Journal of Computational Physics*.

Kim, Y.-J., F. X. Giraldo, M. Flatau, C.-S. Liou, and M. S. Peng, 2008: A sensitivity study of the Kelvin wave and the Madden-Julian Oscillation in aquaplanet simulations by the Naval Research Laboratory Spectral Element Atmospheric Model. *Journal of Geophysical Research*, **113**, 1–16.

Klemp, J. B. and R. B. Wilhelmson, 1978: The Simulation of Three-Dimensional Convective Storm Dynamics. *Journal of the Atmospheric Sciences*, **35 (6)**, 1070–1096.

Özgökmen, T. M., P. F. Fischer, J. Duan, and T. Iliescu, 2004: Three-Dimensional Turbulent Bottom Density Currents from a High-Order Nonhydrostatic Spectral Element Model. *Journal of Physical Oceanography*, **34 (9)**, 2006.

Rotunno, R., J. B. Klemp, and M. L. Weisman, 1988: A Theory for Strong, Long-Lived Squall Lines. *Journal of the Atmospheric Sciences*, **45 (3)**, 463–485.

Skamarock, W. C., J. B. Klemp, J. Dudhia, D. O. Gill, D. M. Barker, W. Wang, and J. G. Powers, 2005: A description of the Advanced Research WRF version 2.

Straka, J. M., R. B. Wilhelmson, L. J. Wicker, J. R. Anderson, and K. K. Droegemeier, 1993: Numerical solutions of a non-linear density current: A benchmark solution and comparisons - Straka - 2005 - International Journal for Numerical Methods in Fluids -

Wiley Online Library. *International Journal for Numerical Methods in Fluids*, **17 (1)**, 1–22.

Weisman, M. L., J. B. Klemp, and R. Rotunno, 1988: Structure and evolution of numerically simulated squall lines. *Journal of the Atmospheric Sciences*, **45 (14)**.

Weisman, M. L. and R. Rotunno, 2004: A Theory for Strong Long-Lived Squall Lines Revisited. *Journal of the Atmospheric Sciences*, **61 (4)**, 361.

Weisman, M. L., W. C. Skamarock, and J. B. Klemp, 1997: The Resolution Dependence of Explicitly Modeled Convective Systems. *Monthly Weather Review*, **125 (4)**, 527.

28

List of Tables

Number of elements (h) in horizontal/vertical

Polynomial order (p)	6/4	8/4	10/5	12/6	16/8	20/10	24/12	30/15	40/20	48/24	60/30	80/40	120/60
10	4000/600 0.50 (**79**)	*3000/600* 0.50 (**80**)	2400/480 0.50 (**81**)	*2000/400* 0.50 (**82**)	1500/300 0.50 (**83**)	1200/240 0.25 (**84**)	*1000/200* 0.25 (**85**)	800/160 0.25 (**86**)	600/120 0.25 (**87**)	*500/100* 0.20 (**88**)	400/80 0.20 (**89**)	300/60 0.10 (**90**)	200/40 0.10 (**91**)
9	4444/667 0.50 (**66**)	3333/667 0.50 (**67**)	2667/533 0.50 (**68**)	2222/444 0.50 (**69**)	1667/333 0.50 (**70**)	1333/267 0.50 (**71**)	1111/222 0.25 (**72**)	889/178 0.25 (**73**)	667/133 0.25 (**74**)	556/111 0.20 (**75**)	444/89 0.20 (**76**)	333/67 0.10 (**77**)	222/44 0.10 (**78**)
8	5000/750 0.50 (**53**)	3750/750 0.50 (**54**)	*3000/600* 0.50 (**55**)	2500/500 0.50 (**56**)	1875/375 0.50 (**57**)	1500/300 0.50 (**58**)	1250/250 0.25 (**59**)	*1000/200* 0.25 (**60**)	750/150 0.25 (**61**)	625/125 0.25 (**62**)	*500/100* 0.20 (**63**)	375/75 0.10 (**64**)	250/50 0.10 (**65**)
7	5714/857 0.50 (**40**)	4286/857 0.50 (**41**)	3429/686 0.50 (**42**)	2857/571 0.50 (**43**)	2143/429 0.50 (**44**)	1714/343 0.50 (**45**)	1429/286 0.50 (**46**)	1143/229 0.25 (**47**)	857/171 0.25 (**48**)	714/143 0.25 (**49**)	571/114 0.25 (**50**)	429/86 0.20 (**51**)	286/57 0.10 (**52**)
6	6667/1000 0.50 (**27**)	5000/1000 0.50 (**28**)	4000/800 0.50 (**29**)	3333/667 0.50 (**30**)	2500/500 0.50 (**31**)	*2000/400* 0.50 (**32**)	1667/333 0.50 (**33**)	1333/267 0.50 (**34**)	*1000/200* 0.25 (**35**)	833/167 0.25 (**36**)	667/133 0.25 (**37**)	*500/100* 0.20 (**38**)	333/67 0.20 (**39**)
5	8000/1200 0.50 (**14**)	6000/1200 0.50 (**15**)	4800/960 0.50 (**16**)	4000/800 0.50 (**17**)	*3000/600* 0.50 (**18**)	2400/480 0.50 (**19**)	*2000/400* 0.50 (**20**)	1600/320 0.50 (**21**)	1200/240 0.25 (**22**)	*1000/200* 0.25 (**23**)	800/160 0.25 (**24**)	600/120 0.25 (**25**)	400/80 0.20 (**26**)
4	10000/1500 0.50 (**1**)	7500/1500 0.50 (**2**)	6000/1200 0.50 (**3**)	5000/1000 0.50 (**4**)	3750/750 0.50 (**5**)	*3000/600* 0.50 (**6**)	2500/500 0.50 (**7**)	*2000/400* 0.50 (**8**)	1500/300 0.50 (**9**)	1250/250 0.25 (**10**)	*1000/200* 0.25 (**11**)	750/150 0.25 (**12**)	*500/100* 0.20 (**13**)

TABLE 1. Table of setup parameters for all the cases as a function of the polynomial order (p) and number of elements in horizontal (h) and vertical. Within each cell, the middle two numbers represent average horizontal and vertical grid spacing ($\overline{\Delta x}/\overline{\Delta z}$ in meters) and the bottom number is the time step (Δt in seconds). The bold number in parentheses represents the experiment number. The nominal resolution for a subset of cases is emphasized by italics ($\overline{\Delta x}$=3000, 2000, 1000 and 500 m).

Height (m)	0	500	1000	1500	2000
CAPE (J/kg)	2383	2426	2781	1968	1133

TABLE 2. Initial air-parcel heights and corresponding CAPE values.

p	$\Delta x_{max}/\Delta x_{min}$	$\Delta x_{max}/\overline{\Delta x}$	$\Delta x_{min}/\overline{\Delta x}$
4	1.90	1.31	0.69
5	2.43	1.43	0.59
6	2.76	1.41	0.51
7	3.26	1.47	0.45
8	3.62	1.45	0.40
9	4.11	1.49	0.36
10	4.48	1.48	0.33
20	8.77	1.53	0.17

TABLE 3. Polynomial orders (p) and associated nodal spacing ratios.

List of Figures

5   Normalized l_2 norm of momentum flux for the two–dimensional linear hydrostatic mountain wave simulations as a function of normalized computational time. Results obtained with the SE model are: solid black line (p=4), dashed dark grey (p=6), dot–dashed medium gray (p=8) and dotted lightgrey (p=10). The lightest gray line with triangles is for the finite–difference model. Simulations with the same nominal resolutions are grouped together and represented with small circles (0.5 km), circles with wide rings (1.0 km), circles with thick inner and thin outer rings (2.0 km) and circles with two thick rings (3.0 km).   40

6   Vertical cross sections of the squall line evolution as depicted by a simulation with p=8, h=30, $\overline{\Delta x}$=1 km $\overline{\Delta z}$=0.2 km at a) 900, b) 1800, c) 4800 and d) 9000 s. Filled contours represent equivalent potential temperature perturbation (c.i. 3 K), positive values with dark and negative values with light contour lines. The interval centered around zero ($[-3, 3]$) is omitted). The cloud water mixing ratio ($q_c = 10^{-5}$) in thick black line represents the outline of the cloud. The bottom portion of each panel shows rain water accumulation as a function of distance. Only a smaller subset of the full domain is shown to emphasize the details.   41

7   Same as Fig. 6, but at time t=6000 s and for cases a) p=4, h=60, b) p=5, h=48, c) p=6, h=40, d) p=8, h=30, e) p=10, h=24 and f) p=20, h=12. All cases have the same nominal horizontal resolution $\overline{\Delta x}$=1 km and time step Δt=0.25 s.   42

8   Same as Fig. 6, but at time t=6000 s and for cases a) h=10, $\overline{\Delta x}$=3.0 km, Δt=0.5 s, b) h=20, $\overline{\Delta x}$=1.5 km, Δt=0.5 s, c) h=40, $\overline{\Delta x}$=0.75 km, Δt=0.25 s and d) h=80, $\overline{\Delta x}$=0.375 km, Δt=0.1 s . All cases with p=8.   43

9   a) Total rain accumulation (in mm) in 6 hours averaged over the whole domain, b) Maximum rain rate (in kg m^{-1} s^{-1}) and c) Maximum vertical velocities (in m s^{-1}), as a function of the polynomial order (p) and number of elements in horizontal (h) for the squall line simulations. Curved black lines represent constant nominal horizontal resolution ($\overline{\Delta x}$, or constant number of nodal points in the horizontal direction).   44

10   Power spectra for simulations with p=8 and varying nominal resolutions:$\overline{\Delta x}$=3.0 km (thickest light grey line), $\overline{\Delta x}$=1.5 km (thick grey line), $\overline{\Delta x}$=0.75 km (thin dark grey line) and $\overline{\Delta x}$=0.375 km (thinnest black line). Panel a) is for the control squall line simulations and panel b) is for the "dry" squall line (see text for further explanation). The spectra are averaged over height (0-12 km, with 0.5 km increment) and time (0-4 h, with 300 s increment).   45
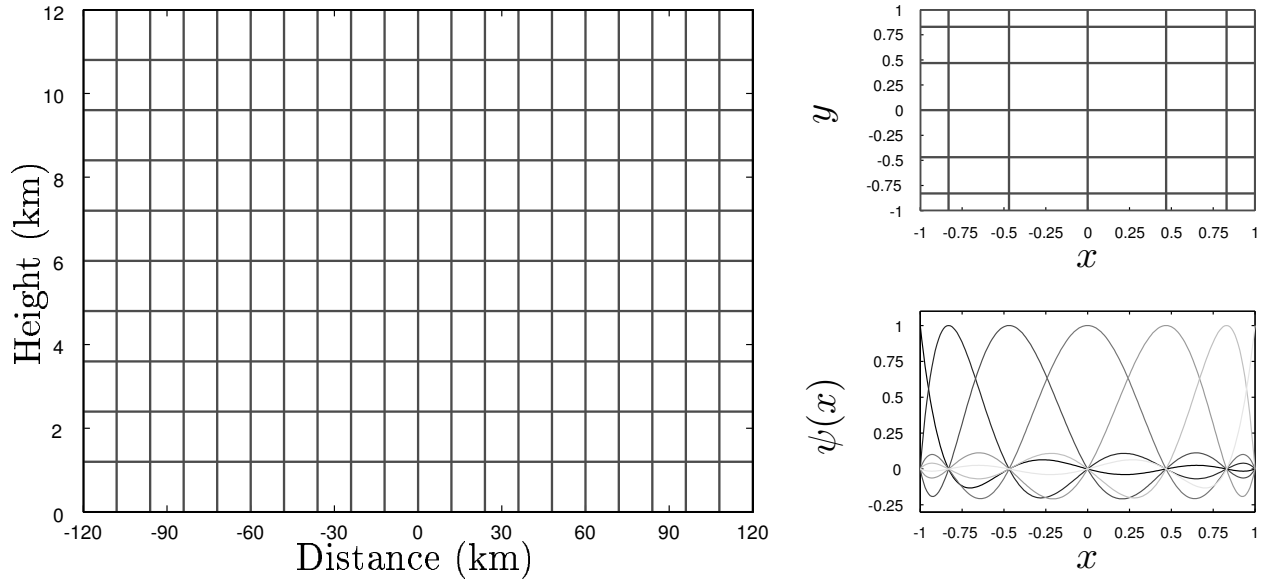
FIG. 1. An example of element decomposition of the computational domain for a case with polynomial order, p=6, number of elements in horizontal h=20 and 10 in vertical (left panel). Distribution of LGL nodal points within a canonical element with p=6 (top right panel). Basis functions $\psi_1, \ldots, \psi_7$ for p=6 (bottom right panel).
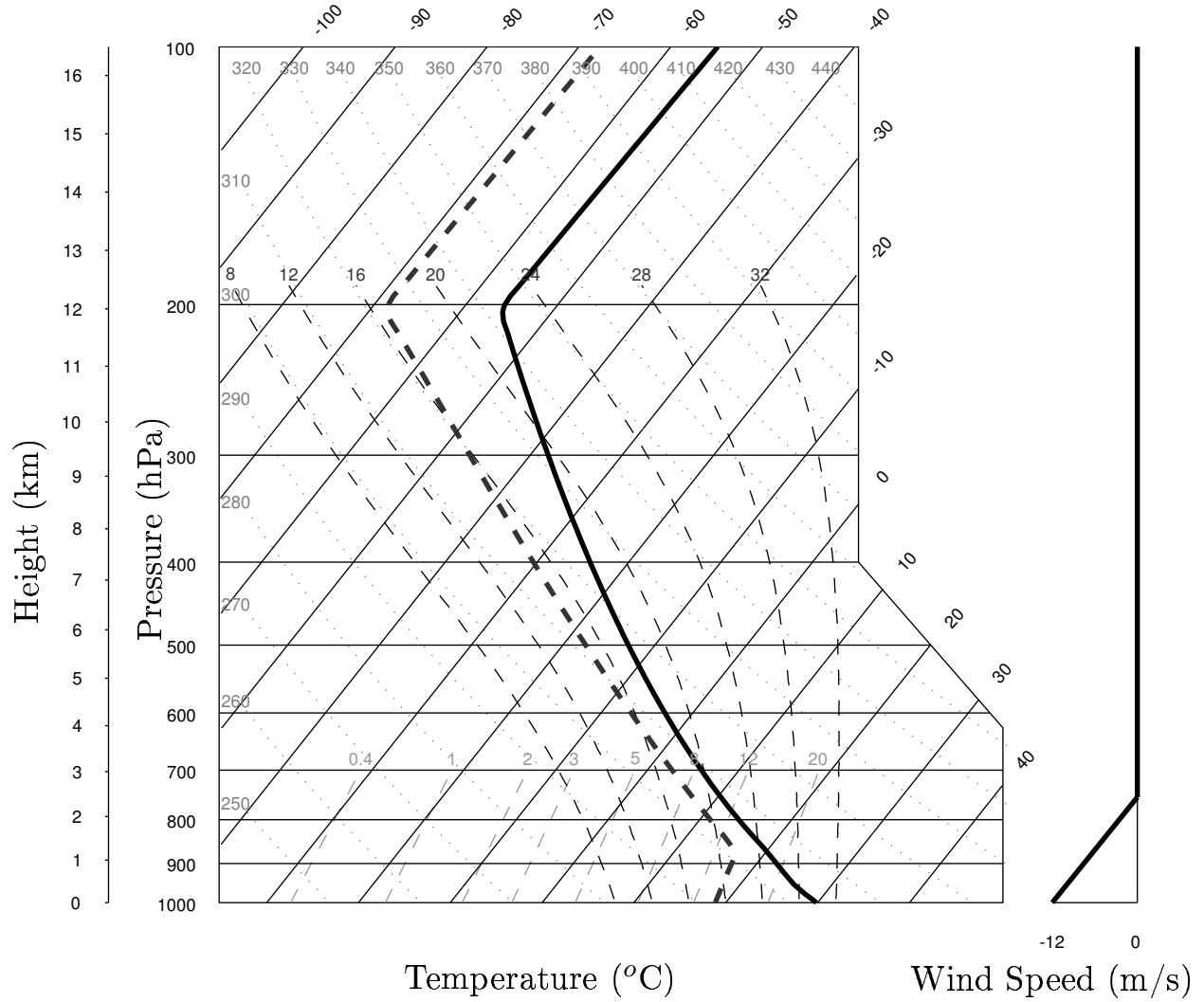
FIG. 2. The synthetic sounding used to initialize the model. Temperature and dew point temperature are represented by a thicker, solid black and dashed, grey line, respectively. The wind speed profile is given on the right panel.
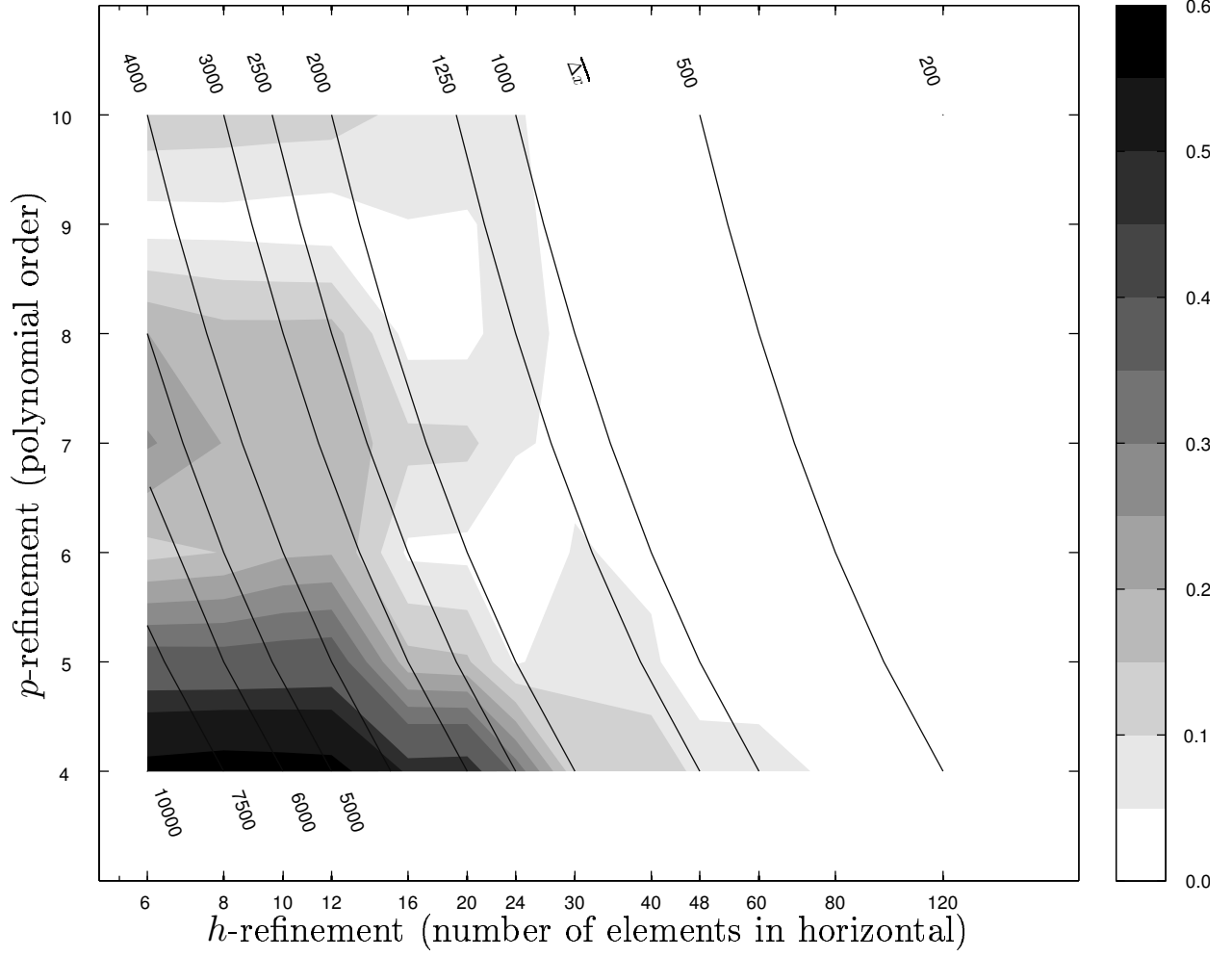
FIG. 3. Normalized l_2 norm (shaded contours, c.i. 0.05) of the vertical momentum flux as a function of the polynomial order (p) and number of elements in horizontal (h) for the dry, linear, hydrostatic mountain wave case. Curved black lines represent constant nominal horizontal resolution ($\overline{\Delta x}$, or constant number of nodal points in the horizontal direction).
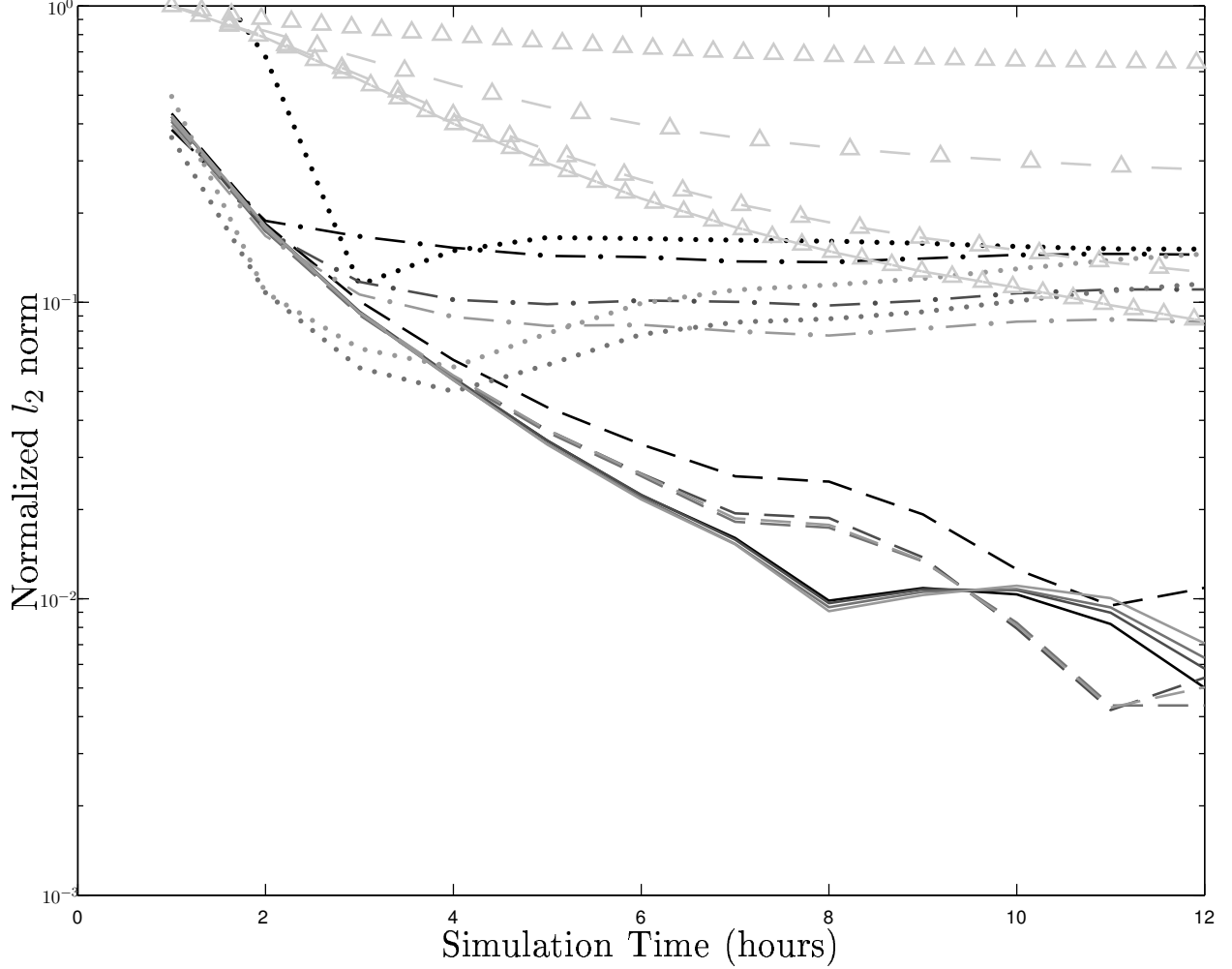
FIG. 4. Time evolution of the normalized l_2 norm of momentum flux for the two–dimensional linear hydrostatic mountain wave simulations (output every hour, starting at $t = 1$ h). Results based on simulations with the same horizontal resolution are grouped by a line type: dotted (3.0 km),dash-dotted (2.0 km),dashed (1.0 km), and solid (0.5 km).Shades of gray depict the polynomial order of basis functions: black ($p = 4$), dark gray ($p = 6$),medium gray ($p = 8$),and light gray ($p = 10$).In addition, results obtained with the finite–difference model (lightest gray) have added diamonds, which also replace dots in corresponding line styles.

39
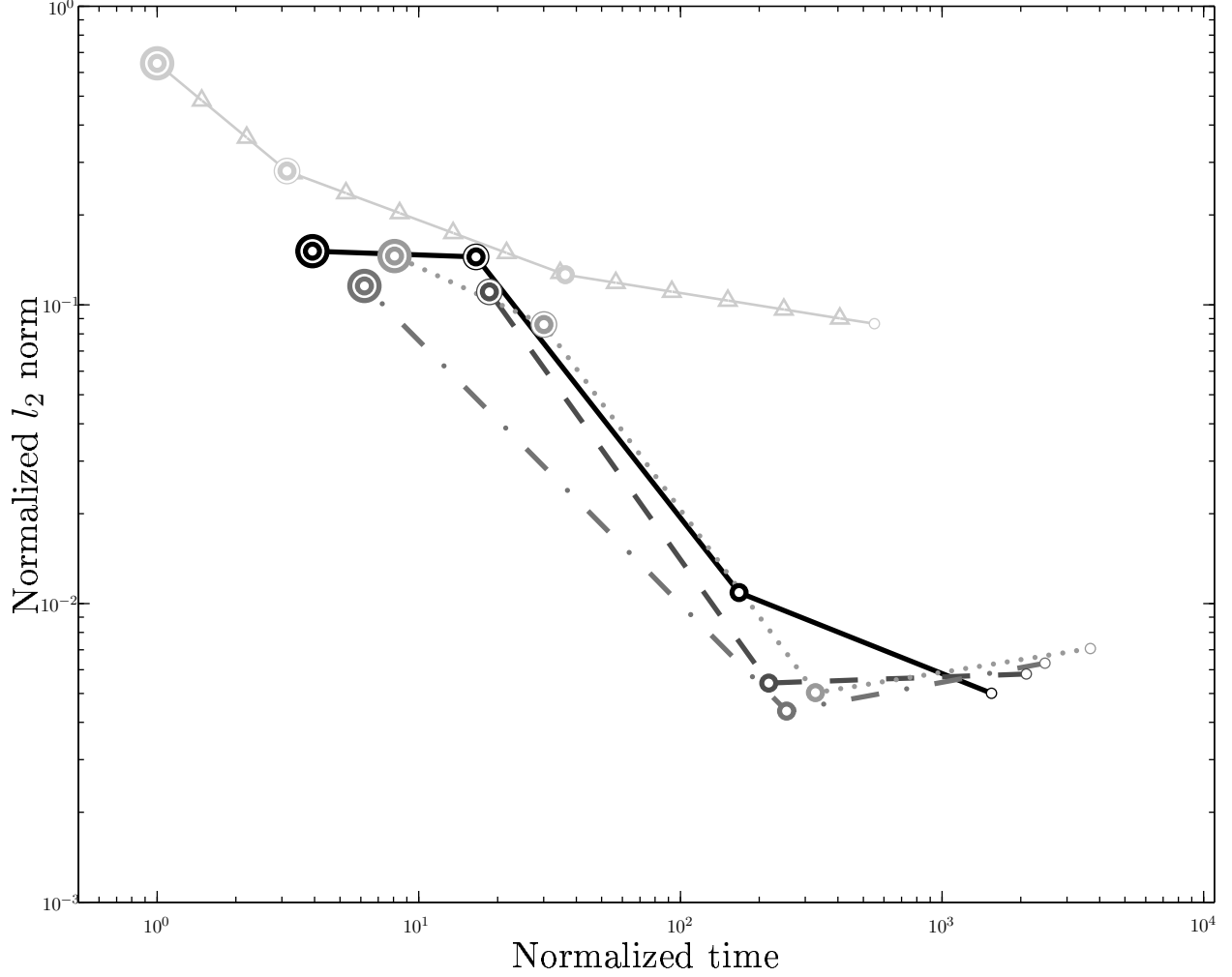
FIG. 5. Normalized l_2 norm of momentum flux for the two–dimensional linear hydrostatic mountain wave simulations as a function of normalized computational time. Results obtained with the SE model are: solid black line (p=4), dashed dark grey (p=6), dot–dashed medium gray (p=8) and dotted lightgrey (p=10). The lightest gray line with triangles is for the finite–difference model. Simulations with the same nominal resolutions are grouped together and represented with small circles (0.5 km), circles with wide rings (1.0 km), circles with thick inner and thin outer rings (2.0 km) and circles with two thick rings (3.0 km).

FIG. 6. Vertical cross sections of the squall line evolution as depicted by a simulation with $p=8$, $h=30$, $\overline{\Delta x}=1$ km $\overline{\Delta z}=0.2$ km at a) 900, b) 1800, c) 4800 and d) 9000 s. Filled contours represent equivalent potential temperature perturbation (c.i. 3 K), positive values with dark and negative values with light contour lines. The interval centered around zero ($[-3, 3]$) is omitted). The cloud water mixing ratio ($q_c = 10^{-5}$) in thick black line represents the outline of the cloud. The bottom portion of each panel shows rain water accumulation as a function of distance. Only a smaller subset of the full domain is shown to emphasize the details.
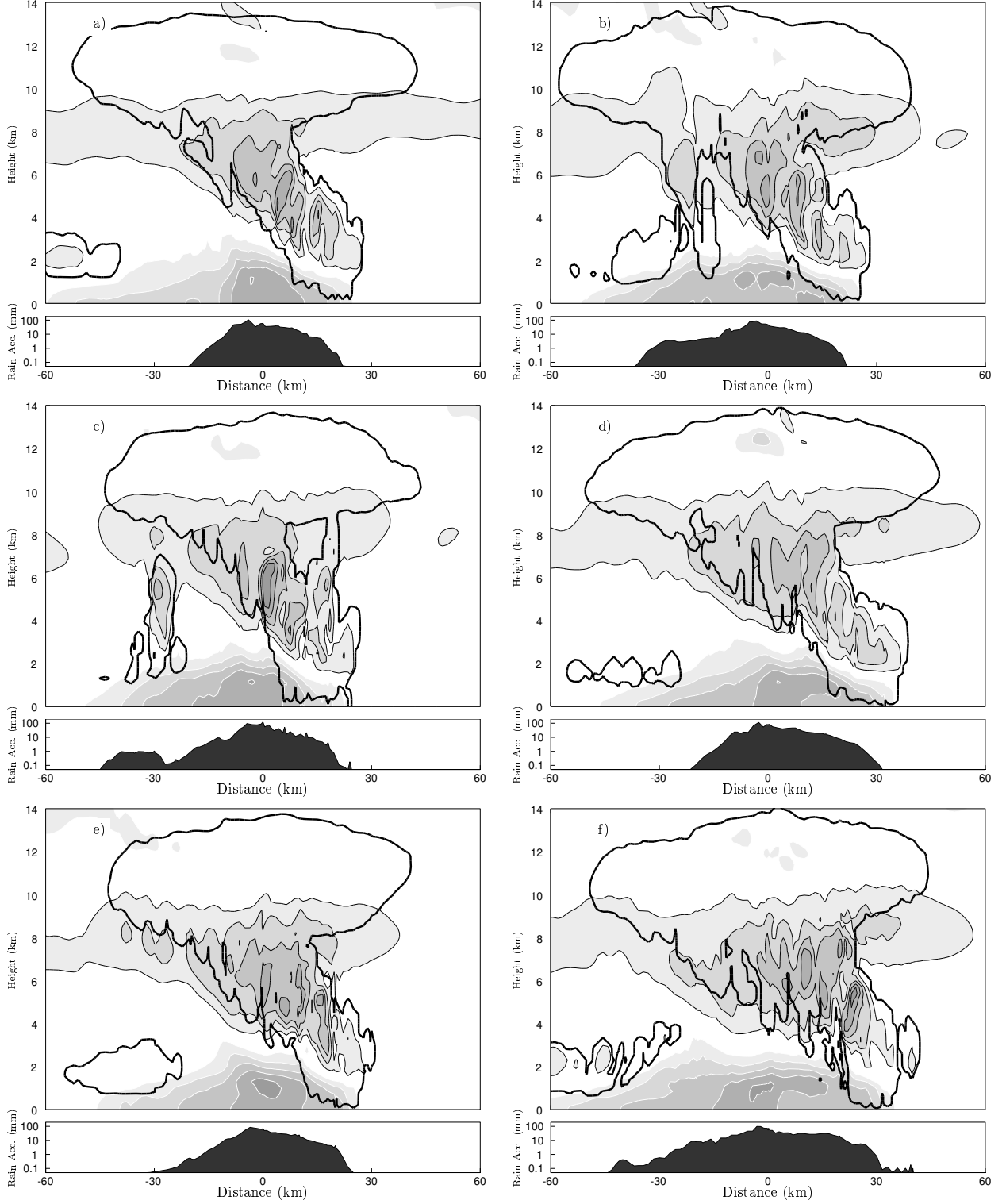
FIG. 7. Same as Fig. 6, but at time t=6000 s and for cases a) p=4, h=60, b) p=5, h=48, c) p=6, h=40, d) p=8, h=30, e) p=10, h=24 and f) p=20, h=12. All cases have the same nominal horizontal resolution $\overline{\Delta x}$=1 km and time step Δt=0.25 s.
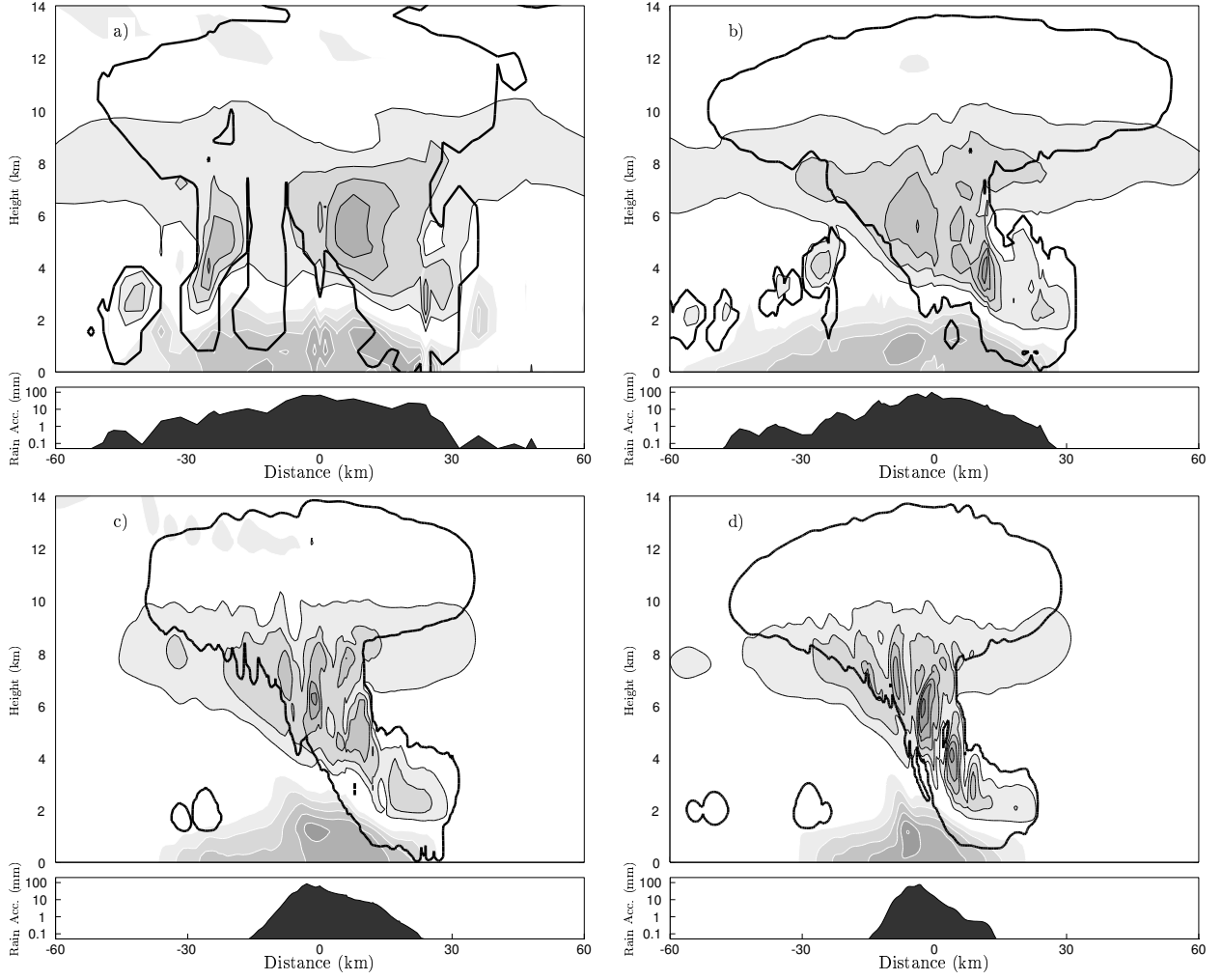
42

FIG. 8. Same as Fig. 6, but at time t=6000 s and for cases a) h=10, $\overline{\Delta x}$=3.0 km, Δt=0.5 s, b) h=20, $\overline{\Delta x}$=1.5 km, Δt=0.5 s, c) h=40, $\overline{\Delta x}$=0.75 km, Δt=0.25 s and d) h=80, $\overline{\Delta x}$=0.375 km, Δt=0.1 s . All cases with p=8.
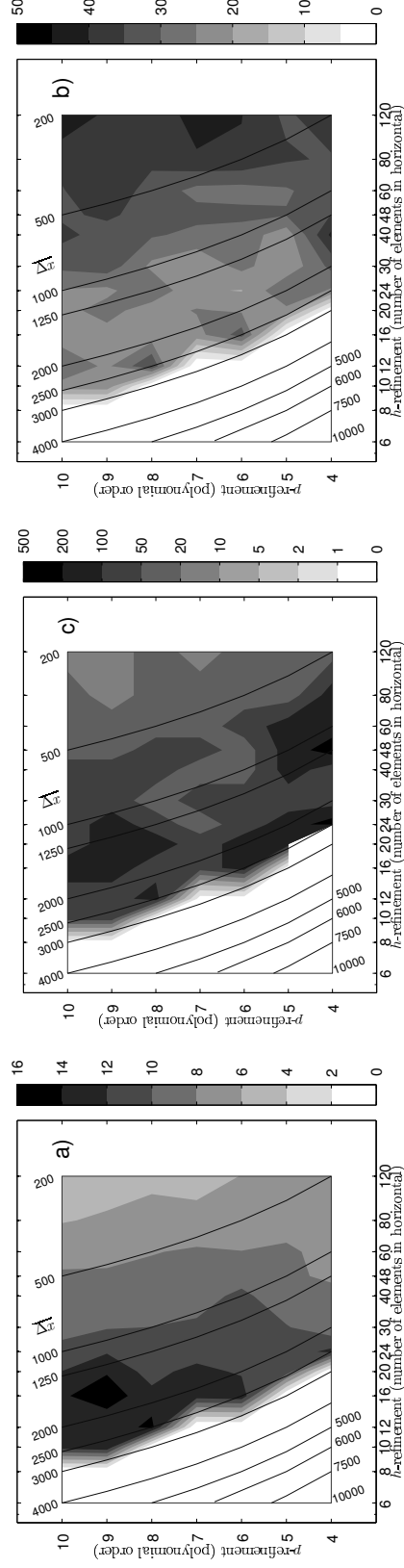
Fig. 9. a) Total rain accumulation (in mm) in 6 hours averaged over the whole domain, b) Maximum rain rate (in kg m^{-1} s^{-1}) and c) Maximum vertical velocities (in m s^{-1}), as a function of the polynomial order (p) and number of elements in horizontal (h) for the squall line simulations. Curved black lines represent constant nominal horizontal resolution ($\overline{\Delta x}$, or constant number of nodal points in the horizontal direction).
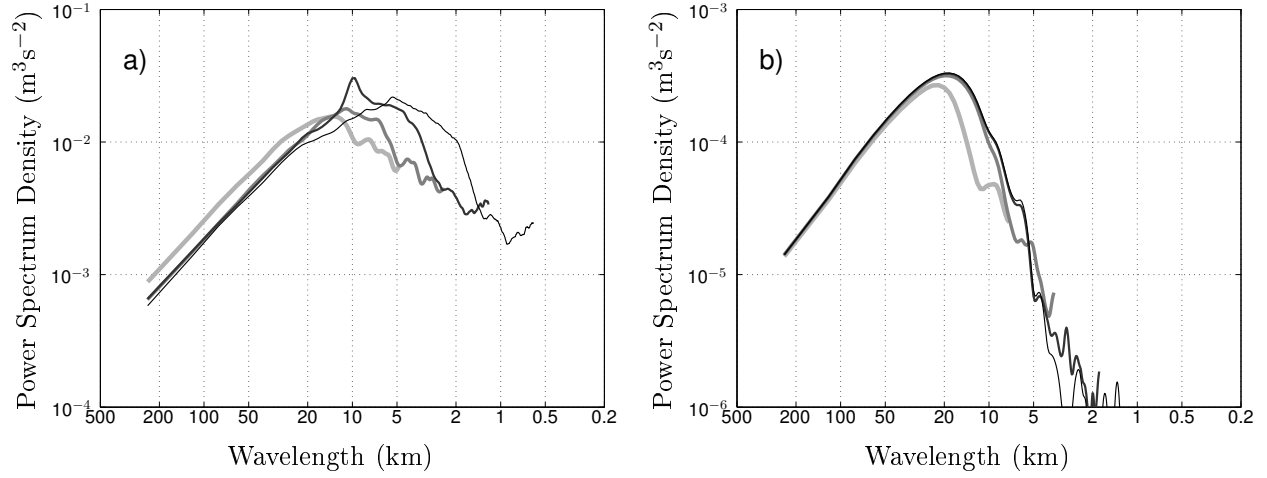
44

FIG. 10. Power spectra for simulations with $p=8$ and varying nominal resolutions:$\overline{\Delta x}$=3.0 km (thickest light grey line), $\overline{\Delta x}$=1.5 km (thick grey line), $\overline{\Delta x}$=0.75 km (thin dark grey line) and $\overline{\Delta x}$=0.375 km (thinnest black line). Panel a) is for the control squall line simulations and panel b) is for the "dry" squall line (see text for further explanation). The spectra are averaged over height (0-12 km, with 0.5 km increment) and time (0-4 h, with 300 s increment).